Performance enhancement of a novel serpentine channel cooled plate used for cooling of Li-ion battery module

Jaffal, Hayder Mohammad; Mahmoud, Nabeel Sameer; Imran, Ahmed Abdulnabi; Hasan, Ala

Published in:
International Journal of Thermal Sciences

DOI:
10.1016/j.ijthermalsci.2022.107955

Published: 01/02/2023

Document Version
Publisher's final version

International Journal of Thermal Sciences 184 (2023) 107955

Contents lists available at ScienceDirect

International Journal of Thermal Sciences

journal homepage: www.elsevier.com/locate/ijts

Performance enhancement of a novel serpentine channel cooled plate used for cooling of Li-ion battery module

Hayder Mohammad Jaffal [a], Nabeel Sameer Mahmoud [b], Ahmed Abdulnabi Imran [b], Ala Hasan [c,*]

[a] Mechanical Engineering Department, College of Engineering, Mustansiriyah University, Baghdad, Iraq
[b] Mechanical Engineering Department, University of Technology, Iraq
[c] VTT Technical Research Centre of Finland Ltd., P.O. Box 1000, FI-02044, VTT, Finland

ARTICLE INFO

Keywords:
Performance enhancement
Cooled plate
Li-ion battery
Liquid–cooling
Serpentine ribbed channel
Rib orientation

ABSTRACT

One of the most significant challenges of battery thermal management system is manifested in maintaining optimal battery performance by keeping the overall battery temperature within a narrow temperature range. The present work aimed to study a novel design of ribbed serpentine channel cooled plate (SCCP) as an effective cooling module of Li-ion battery. The study included a numerical simulation of the effect of the rib orientation (90°, 75°, 60°, and 45°) and the rib shape (semi-circular, trapezoidal, and triangular) on the hydrothermal performance of SCCP. The study was conducted under laminar flow conditions for a Reynolds number range (200–1000) and battery cell discharge rate range (1C–2C). The numerical simulation results were validated against experimental measurements of the performance of a SCCP with semi-circular ribs that rotated by 90°. The validation showed a good agreement with a maximum deviation of 8% and 11% for the Nusselt number and the friction factor, respectively. The results of the study indicated that the ribs play a vital role in improving the heat transfer. It is found that the rib orientation was more effective than the rib shape in enhancing the hydrothermal performance improvement factor. In addition, the triangular rib with 45° orientation showed highest performance improvement factor compared with the other SCCP designs with a value of 1.3.

1. Introduction

Electric vehicles are considered environmentally friendly as they reduce harmful greenhouse gas emissions produced from the use of fossil fuels in traditional petrol-fuel vehicles [1]. Lithium batteries (Li-ion) have received great attention as an efficient energy storage system in electric vehicles due to many desirable features such as high energy density and long cycle life [2]. The excessive amount of heat generated in Lithium batteries causes a thermal runaway phenomenon, which may lead to failure in battery cells. So, an urgent demand for an efficient cooling system is emerged to keep the battery temperature within reasonable limits (20° C - 45° C) [3]. Accordingly, different cooling methods were harnessed to remove the heat from the lithium battery, such as liquid cooling, air cooling [4–8], mist cooling, thermoelectric cooling, and active cooling using phase change materials (PCM) [9–15]. In addition, hybrid methods were used to combine more than one cooling methods [16–19].

As a result of its inexpensive cost, passive methods of improving heat transfer are still in the focus for researchers aiming at improving the performance of different kinds of liquid cooling heat sinks. To achieve this goal, it is imperative to develop a flow distribution method that ensures maximum heat dissipation with least pumping power [20–22]. Liquid cooling using mini-channels has attracted great attention due to its effectiveness in cooling lithium battery cells. Huo et al. [23] and Qian et al. [24] numerically studied the effects of mass flow rate, ambient temperature, number of straight channels, and the direction of flow on the battery temperature rise during 5C discharge rate. The results indicated that the battery's maximum temperature and temperature uniformity decreases as the flow rate and number of channels increase. Monika et al. [25] numerically studied the effect of several design and operation parameters, such as number of straight channels, width of channels, liquid flow rate, discharge rate, coolant temperature, type of coolant, and ambient temperature. The results indicated that as the coolant flow rate increases, the average temperature of the battery unit decreases at the expense of higher pressure drop. Shen et al. [26]

* Corresponding author.
E-mail addresses: jaffal.env@uomustansiriyah.edu.iq (H.M. Jaffal), Nabeel.S.Mahmoud@uotechnology.edu.iq (N.S. Mahmoud), Ahmed.A.Imran@uotechnology.edu.iq (A.A. Imran), ala.hasan@vtt.fi (A. Hasan).

https://doi.org/10.1016/j.ijthermalsci.2022.107955
Received 14 March 2022; Received in revised form 23 August 2022; Accepted 21 September 2022
Available online 5 October 2022

Nomenclatures

A_h	heat transfer area, m^2
A_f	flow area, m^2
B	width of the SCCP, m
Cp	specific heat, $Jkg^{-1}K^{-1}$
D_h	hydraulic diameter, $\frac{4(W_{ch} \cdot H_{ch})}{2(W_{ch}+H_{ch})}$, m
H_{ch}	channel height, m
$\overline{h}$	heat transfer coefficient, $Wm^{-2}K^{-1}$
L	length of the SCCP, m
Lp	length of serpentine path, m
$\dot{m}$	mass flow rate, kg s^{-1}
$\overline{Nu}$	Nusselt number
P	pressure, Pa
q	heat gain, W
$\dot{q}$	battery heat generation, W
q''	heat flux, Wm^{-2}
Re	Reynolds number, $\frac{\rho_f \overline{u} D_h}{\mu_f}$
T	temperature, °C
$\overline{T_s}$	surface temperature, °C
$\overline{u}$	velocity, m s^{-1}
W_{ch}	channel width, m

Greek Symbols

ρ	density, kg m^{-3}
μ	dynamic viscosity, Pa.s
ΔP	pressure drop, (Pi-Po), Pa
ΔT	temperature non-uniformity (TNU), K
λ	thermal conductivity, $Wm^{-1}K^{-1}$
θ	orientation angle,°

Subscripts

b	base
f	fluid
i	inlet
o	outlet
r	ribbed
s	solid

numerically studied the effect of inlet coolant temperatures, number of serpentine channels, configurations, flow rates and discharge rates. The results of the study showed that the best cooling performance is for the channels that are located on the same side with eight serpentine channels. Panchal et al. [27] numerically and experimentally studied the performance of serpentine channel cold plate for turbulent water flow under discharge rates of (1C–2C) and inlet water temperatures (5–15° C). Their results showed that the cold plate temperature increases when both the battery discharge rate and the inlet water temperature are increased. Madani et al. [28] numerically studied the effect of the serpentine channel distribution and the direction of cooling. The results showed that the appropriate flow rate for best heat dissipation depends on the configuration of the cold plate. Sheng et al. [29] numerically studied the improvement of the temperature distribution of serpentine channel liquid cooling plate using dual entrances and outlets. The results showed that the thermal performance of the cooling plate with dual entrances and outlets is superior to that with one entrance and outlet. Panchal et al. [30] studied the average surface temperature distributions for different battery discharge rates (2C and 4C) with varying inlet water temperature (5 °C–35 °C) for zig-zag turn type cold plate using neural network model. The results of this study showed that the surface temperature of the battery is directly proportional with the increase in the battery discharge rates. Deng et al. [31] studied numerically the effects of serpentine channels distribution, flow rate of cooling water, number of cold plates, and cooling direction on the thermal performance of the cooling plate. It was shown that better thermal performance can be achieved by placing more cooling channels in the middle of the battery pack. Chen et al. [32] numerically made a comprehensive analysis of the performance improvement of cooling plate for a lithium-ion battery cell based on the experimental results of the heat generated by a battery cell. They indicated the need to examine the effect of the operational conditions, such as the type and flow rate of the coolant fluid and discharge rate, on the performance of the cooling plate. Mondal et al. [33] numerically studied the effects of vortex generators on improving the thermal performance of the cooling plate used to dissipate heat from the battery. The results showed that adding vortex generators to the cooling plate contributes in an effective increase in the Nusselt number and a significant decrease in the maximum temperature of the battery cell.

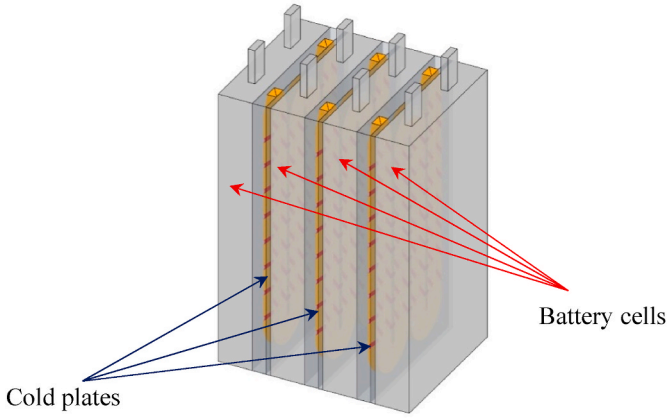

Fig. 1. Arrangement of the cold plates with the battery cells.

Recently, emphasis is placed on studying the effect of inclined ribs as longitudinal vortex generators on improving the heat transfer of straight and serpentine cooling channels. Gao et al. [34] numerically studied the effect of rib angle and rib orientation in a two-pass ribbed U channel using vortex core technique. The combined effects of the rib angle (30°–75°) and rib orientation were tested under turbulent air condition. The results indicated that the main factor to improve the heat transfer is the generation of more secondary flows in the main channel. Brahim [35] numerically studied the effect of the rib's orientation on the heat transfer enhancement in a serpentine square-section channel. To generate a vortex flow, the order of the ribs is arranged in angles of $+45^{\circ}$ or -45° in different rotation forms. A significant improvement in the thermal performance of the serpentine channel was observed due to the use of the oriented ribs. Tanda and Satta [36] studied experimentally and numerically the performance of a rectangular channel with 45° ribs. Their results indicated that when one or two interrupting angled ribs are used, additional vortices are generated between the edges, which contribute in increasing both the heat transfer coefficient and the friction coefficient compared to the standard ribs. Jiang et al. [37] studied numerically and experimentally the effect of V-shaped ribs on improving the thermal performance of a liquid cooled plate used for cooling lithium battery. The effect of the ribs cross-sectional shape (semi-circular, square, trapezoidal and triangular) on the heat transfer and fluid flow characteristics of the V-shaped ribs was studied. Among all the sections of the ribs, the channel with triangular cross-section had the highest thermal performance and the highest pumping power.

From the above studies, it can be concluded that the indirect liquid cooling method is the most effective method for cooling batteries. On the other hand, using inclined ribs is better than vertical ribs to improve the

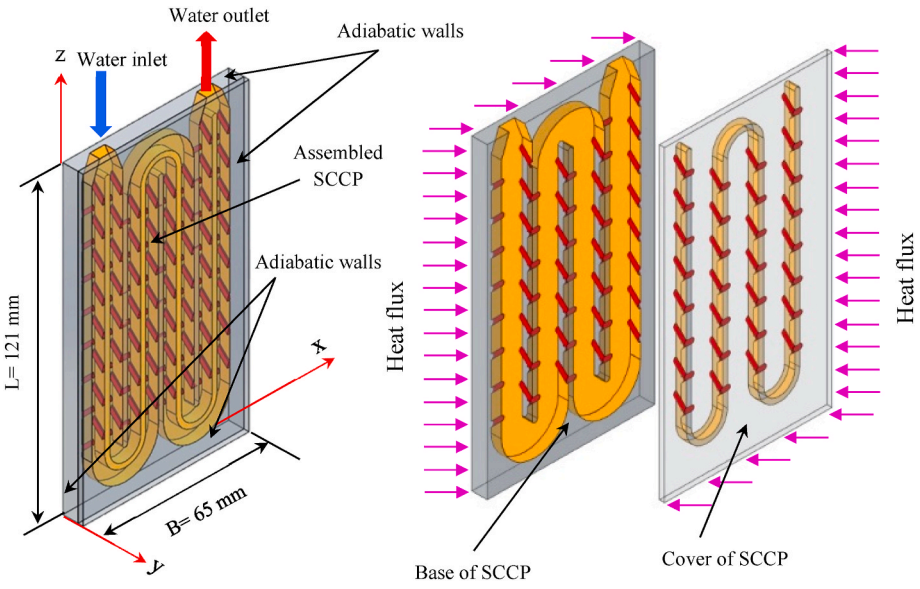

Fig. 2. 3D computational domain of the SCCP-SCR-45°.

performance of various heat sinks. The inclined ribs in one direction were successfully used as a vortex generator to improve the performance of different heat sinks. In the current research, a new type of vortex generators is studied by using a pair of ribs on the channel internal walls oriented in opposite directions to improve the performance of the serpentine channel cooled plate (SCCP) for battery thermal management. In addition, the flow in the main serpentine channel in the new SCCP design is split into two channels. 3D numerical simulation of the SCCP is used to test the effect of the ribs orientation and shape under laminar flow Reynolds number (200–1000) and different battery discharge rates (1C–2C). To demonstrate the reliability of the numerical simulation, a validation was made with experimental results from testing manufactured SCCP with semi-circular ribs at 90° angle.

2. Physical and numerical details

Fig. 1 shows the arrangement of the cooling plates within the battery cells. Fig. 2 illustrates the relation between the simplified computational model of ribbed serpentine channel cooled plate (SCCP) and the two computational domains of fluid or solid. Heat transfer takes place by convection in the cooling water and by conduction in the copper. The external dimensions of the SCCP and the characteristics of the battery cell are as reported by Chen et al. [32]. The SCCP dimensions are length (L) 121 mm, width (B) 65 mm, and thickness (t) 8 mm. Based on the results of the previous studies by Jaffal et al. [38] and Imran et al. [39], which indicated the positive effect of flow fragmentation on improving the hydrothermal performance of serpentine heat sink, the main serpentine channel in the new design of SCCP is divided into two channels to ensure an increase in the heat transfer between the water and the copper plate. The channel dimensions are width (W_{ch}) 5 mm and height (H_{ch}) 4 mm. Water enters the channels at a temperature of 21° C. On both sides of the SCCP, heat is supplied from plate heaters. A constant heat flux ($q'' = \dot{q}/A$) is applied on the two side surfaces of the SCCP with a battery cell capacity of 8 Ah and a range of discharge of 3.6–4.2 V. The battery discharge rates (C-rate) are 1C, 1.2C, 1.5C, 1.8C and 2C for 720, 600, 480, 402 and 360 min, respectively. The C-rate is one of the important characteristics of batteries, which is defined as the rate of electrical energy consumption from the battery during a specified time duration. It is a measure of the rate at which a battery is discharged relative to its maximum capacity. For example, a 1C rate means that the entire battery will be discharged in 1 h, which is equal to a discharge current of 100 Amps for a 100 Amp-hours capacity battery. As the C-rate increases, the battery run-time decreases. The cooling water velocity is set at the inlet of the channels according to the required Reynolds number range of 200–1000. When water passes through the channels, heat is rejected from the copper plate, leading to an increase in the water temperature. Ribs in different orientations are added to the walls of the channels resulting in generating secondary flow in both transverse and longitudinal directions and, therefore, producing better fluid mixing. Consequently, the boundary layer is broken, leading to improving the heat transfer, which is accompanied by increase in the pressure drop through the channels.

The ribs are in a staggered arrangement on the two opposite walls of the channel and their orientation on one wall is in opposite direction to the orientation on the opposite wall as shown in Fig. 3(a). The extension length on the internal wall for the rib with a smaller angle is longer than that for a larger angle and as shown in Fig. 3(b). The ratio of these extension lengths for rib angles of 75°, 60° and 45° are, respectively, 3.5%, 15.5% and 41% longer than that for 90°. Three different rib shapes are studied: semi-circular (SCR), trapezoidal (TRAP) and triangular (TRAN) as shown in Fig. 3(c).

In the numerical analysis, the 3D governing equations for the flow and temperature field are used. The flow is considered a steady, incompressible, and laminar flow. In accordance with the aforementioned assumptions, the following continuity, momentum, and energy equations for laminar flow through the channels of the SCCP are resolved [40]:

$$\nabla.\left(\rho_f \vec{U}\right) = 0 \tag{1}$$

$$\vec{U}.\nabla.\left(\rho_f \vec{U}\right) = -\nabla P + \nabla.\left(\mu_f \nabla \vec{U}\right) \tag{2}$$

$$\vec{U}.\nabla.\left(\rho_f C_{P,f} T\right) = \nabla.\left(\lambda_f \nabla T\right) \tag{3}$$

For the solid domain (copper), the energy equation is

$$\nabla.(\lambda_s \nabla T) = 0 \tag{4}$$

where $\vec{U}$ is the velocity vector, P is the static pressure, T is the temperature, while ρ_f, μ_f, $C_{P,f}$, and λ_f are the density, dynamic viscosity, specific heat, and thermal conductivity of the fluid, respectively, and λ_S is the thermal conductivity of the solid.

Sets of boundary conditions are applied to complete the solution. To acquire accurate solutions, the boundary conditions must be carefully

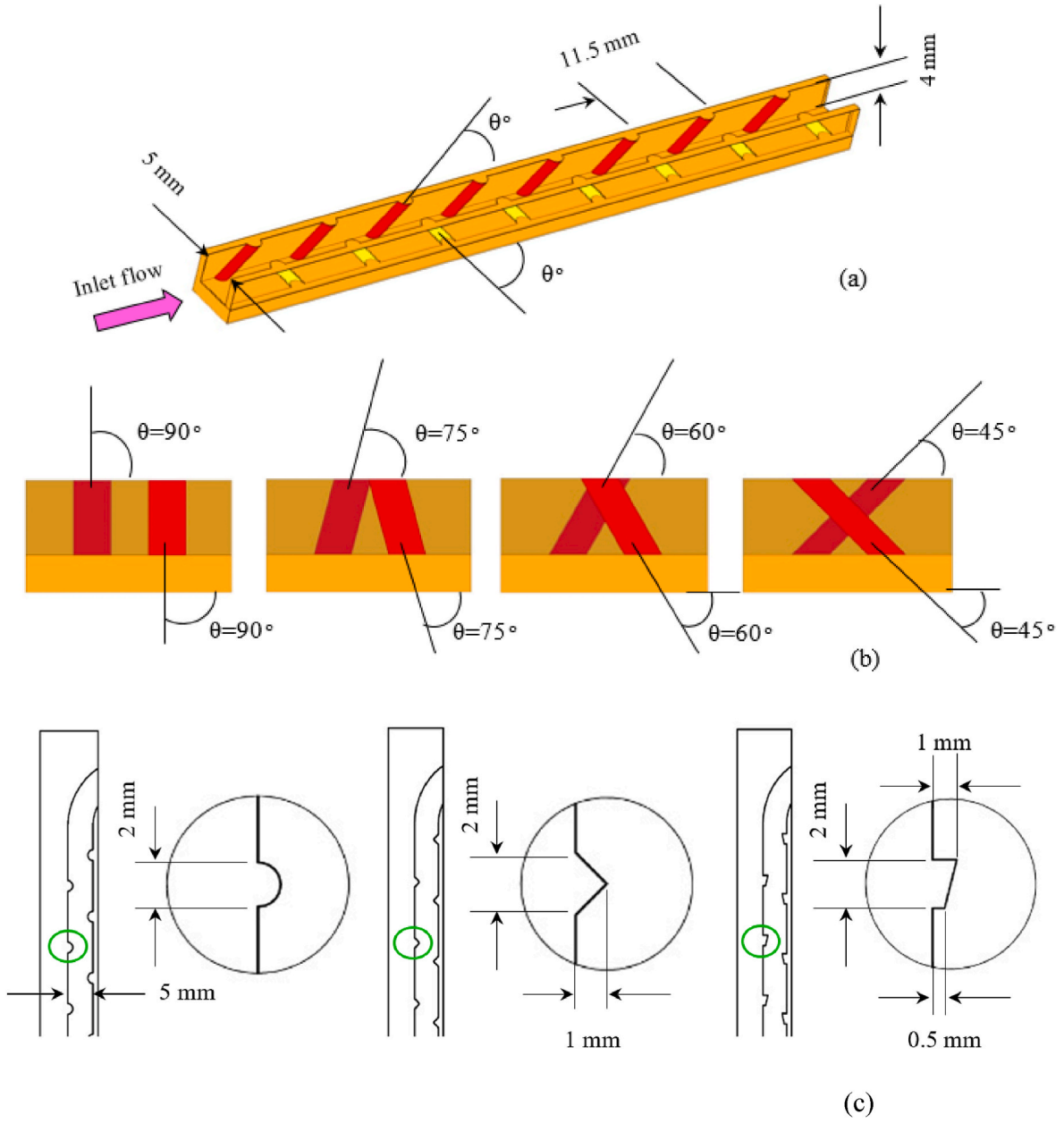

Fig. 3. Schematic view of the rib orientations with respect to the flow inside the channel (a), side view of the channel showing the ribs on the two opposite sides of the channel (b), and the cross-sections of the rib shapes (semi-circular, triangular and trapezoidal) (c).

Table 1
Hydrothermal boundary conditions.

	boundary condition type	hydrothermal boundary condition
SCCP inlet	Velocity inlet	$w = V_{in}, u = v = 0$ $T_f = T_{in} = 21\,^{\circ}C, -\lambda_s \frac{\partial T_s}{\partial z} = 0$
SCCP left and right walls	Heat flux	$u = v = w = 0$ $\lambda_s \frac{\partial T_S}{\partial y} = q''$
Internal channel walls	Fluid-solid interface	$u = v = w = 0$ $-\lambda_f \nabla T_f = -\lambda_s \nabla T_s$
SCCP side walls	Adiabatic and non-slip	$u = v = w = 0$ $-\lambda_f \nabla T_f = 0, -\lambda_s \nabla T_s = 0$
SCCP outlet	Pressure outlet	$P = P_{out} = 1\ atm$ $-\lambda_f \frac{\partial T_f}{\partial z} = 0, -\lambda_s \frac{\partial T_s}{\partial z} = 0$

specified and their usage must consider the rules of physics. The boundary conditions are set to be identical with the real states of flow used in the experimental tests. The boundary conditions for both fluid flow and heat transfer problems have two types: hydraulic and thermal boundary conditions. The boundary conditions in every region of the SCCP are illustrated in Fig. 2 and Table 1. Since the SCCP is located on the two sides of the battery cells, heat flux was applied from the left- and right-side walls of the SCCP. At the entrance to the SCCP, a uniform fluid velocity and temperature are used. In the outlet of the SCCP, zero relative pressure is applied. A non-slip condition is applied on all surfaces. At the internal channel surfaces, conjugate boundary condition is applied (heat transfer from solid to fluid at the interface surfaces). Also, on all SCCP walls, the thermal insulation limit condition (adiabatic) is applied except for the sides on which the heat flux is applied.

To enhance the accuracy of the numerical simulation, a tetrahedron grid is developed and the grid is refined in the copper–water contact regions. The governing equations with their boundary conditions are

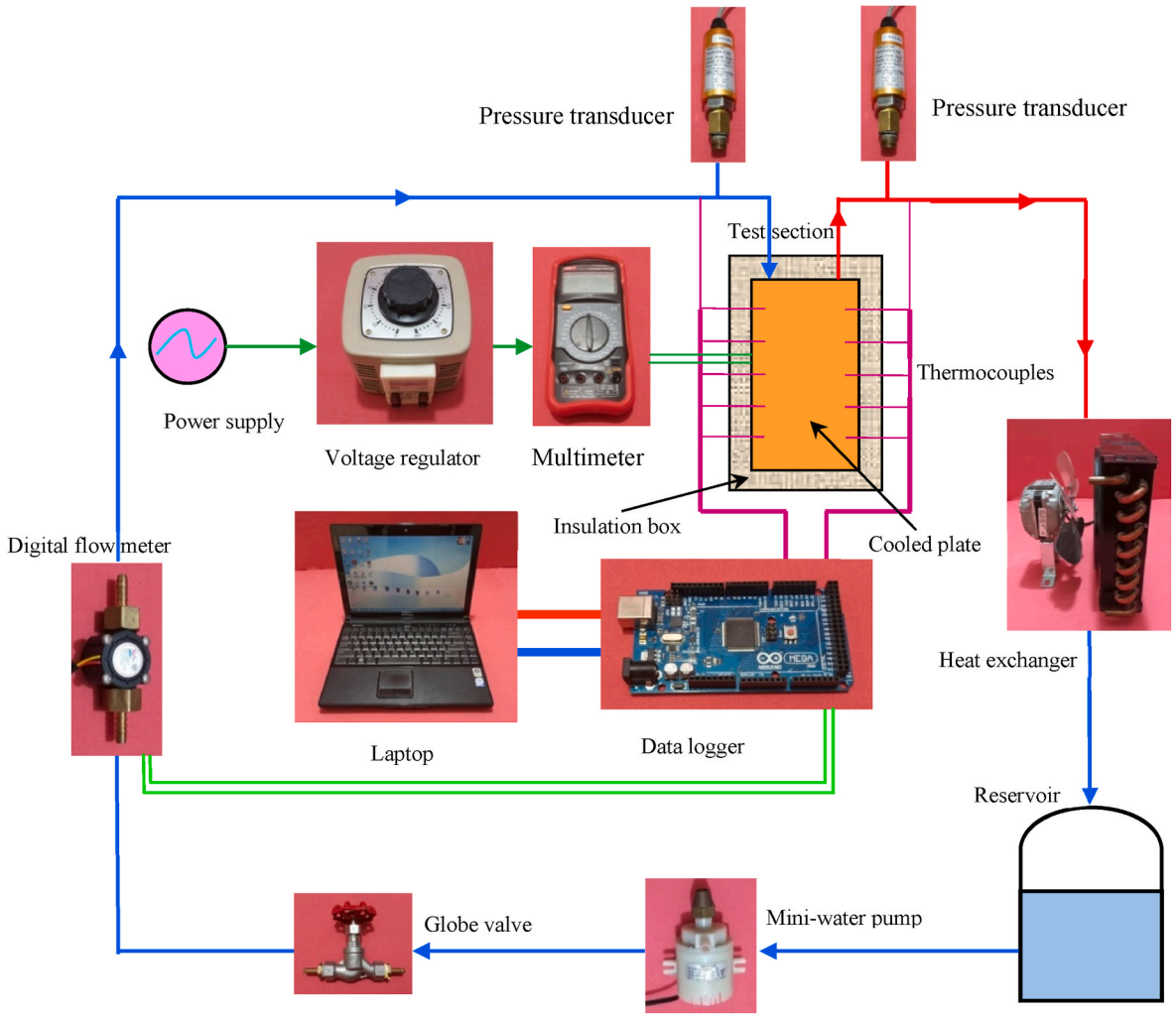

Fig. 4. Schematic of the complete experimental testing system.

numerically solved using a finite volume technique. ANSYS-Fluent (version 18.0) software is utilized to obtain the iterative solution for the algebraic equations. A laminar model is constructed to calculate the flow domain. The SIMPLE algorithm is used in coupling velocity and pressure. Energy and momentum are discretized with a second-order upwind scheme. In the simulation, the solution becomes convergent when the residuals are under 10^{-6}.

3. Experimental details

3.1. Test device components and SCCP manufacturing

The general schematic arrangement of the equipment is depicted in Fig. 4. The major components of the apparatus include a test loop, a test section, and the SCCP.

The test loop consists of a reservoir, a mini-water pump (model G-P 3360 working on DC 12 V, 300 mA, power 7 W, maximum discharge of

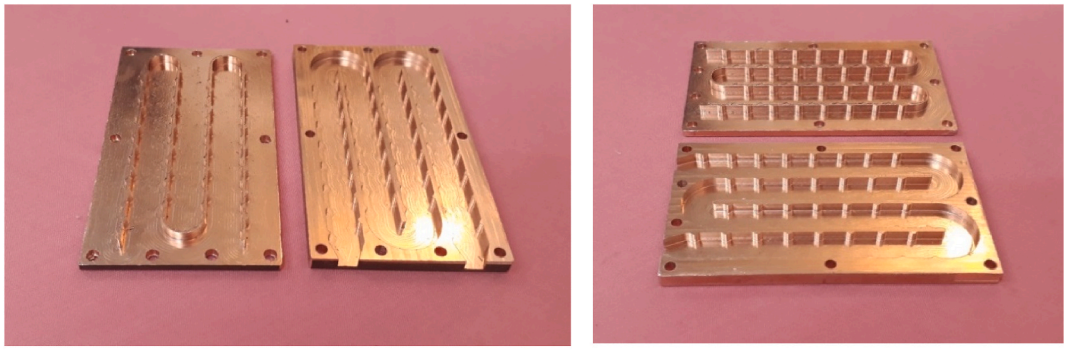

Fig. 5. Views of the manufactured two parts of SCCP-SCR-90°.

Table 2
Geometrical parameters of the manufactured SCCP.

Parameter	Dimensions (mm)
SCCP length	121
SCCP width	65
SCCP thickness	8
Channel width	5
Channel height	4
Rib diameter	2
Space between two ribs	11.5

550 l/h and 1.2 m head), and a flow measurement system. Distilled coolant water from the reservoir is driven by the pump inside the piping through the SCCP where it absorbs heat from the test section leading to an increase in its temperature and returns back to the reservoir. To provide a smooth and steady flow over a wide range of flow rates, the test loop is modified to incorporate a globe valve upstream of the digital flowmeter to control the water flow at different volumetric flow rates. The digital flowmeter range is from 0.1 to 3 l/min with an accuracy of ±0.1%.

The test section comprises the SCCP copper test block and an insulation box made from Teflon™, which consists of a base and a cover that are tightly assembled. The SCCP is placed inside it and used for isolating and preventing heat from leaking into the atmosphere. The SCCP serpentine channels are manufactured by computer numerical control (CNC) machine from two rectangular copper blocks with dimensions of 65 mm (width) and 221 mm (length). The used copper has a density of 8960 kg/m^3 and thermal conductivity of 387.6 W/(m.K). In the original block, the wide serpentine channel was drilled on the walls, and vertical semi-circular ribs were installed, while in the cover block there is a ribbed serpentine fin that divides the wide serpentine channel into two equal ribbed channels. The final appearance of the two copper parts of the SCCP is shown in Fig. 5. Table 2 shows the geometrical parameters of the manufactured SCCP. To ensure that no leakage will occur when the flow moves from the pump, a rubber gasket is placed between the two pieces of the SCCP. The two pieces of the SCCP are tightly assembled with bolts and nuts. The schematic of the test section components and the details of its assembly are shown in Fig. 6. To supply heat, two plate heaters with a maximum power of 200 W are attached to the walls of the SCCP. The plat heaters are controlled by a voltage regulator to provide the desired heat flux. A bench type multi-digital meter is used to measure the heaters power by measuring the voltages and input current. The test section includes inlet and outlet ports for the water, digital water pressure drop transducers (maximum pressure 2 bars with ±0.1% accuracy), and two ports for water temperature measurement over the channel. Two thermocouples type-K are embedded into the ports to measure the temperature of the water at the inlet and outlet of the test section. In addition, ten thermocouples type-K were placed on the base (five thermocouples on each side) to measure the average surface temperature of the SCCP. The measuring tools were calibrated and connected to a data logger and a laptop. The accuracy of the calibrated thermocouples was ±0.05°C. The water flowing in the test section is heated and then flows in a small heat exchanger, which cools the water, and the heat is dissipated into the atmosphere. The cooled water flows back to the reservoir and is then driven by the pump into the SCCP in a closed loop.

3.2. Data reduction

In order to evaluate the thermal/hydraulic performance of the SCCP, several performance parameters are adopted.

One of the most important parameters that are used to compare the thermal performance is the Nusselt number, which is calculated as follows [41,42]:

$$\overline{Nu} = \frac{\overline{h} \cdot D_h}{\lambda_f} = \frac{q \cdot D_h}{A_h \cdot \Delta T_{lm} \cdot \lambda_f} \tag{5}$$

where $\overline{h}$ is the convection heat transfer coefficient, q is heat gain, D_h is channel hydraulic diameter, A_h is convective heat transfer area, ΔT_{lm} is logarithmic mean temperature difference and λ_f is and thermal conductivity of the fluid.

The heat gain by the fluid flow through the SCCP can be calculated as:

$$q = \rho_f Q C_{p,f} \left(T_{f,o} - T_{f,i}\right) = \overline{h} A_h \Delta T_{lm} \tag{6}$$

where ρ_f, Q, $C_{p,f}$, $T_{f,o}$ and $T_{f,i}$ are, respectively, the fluid density, flow rate,

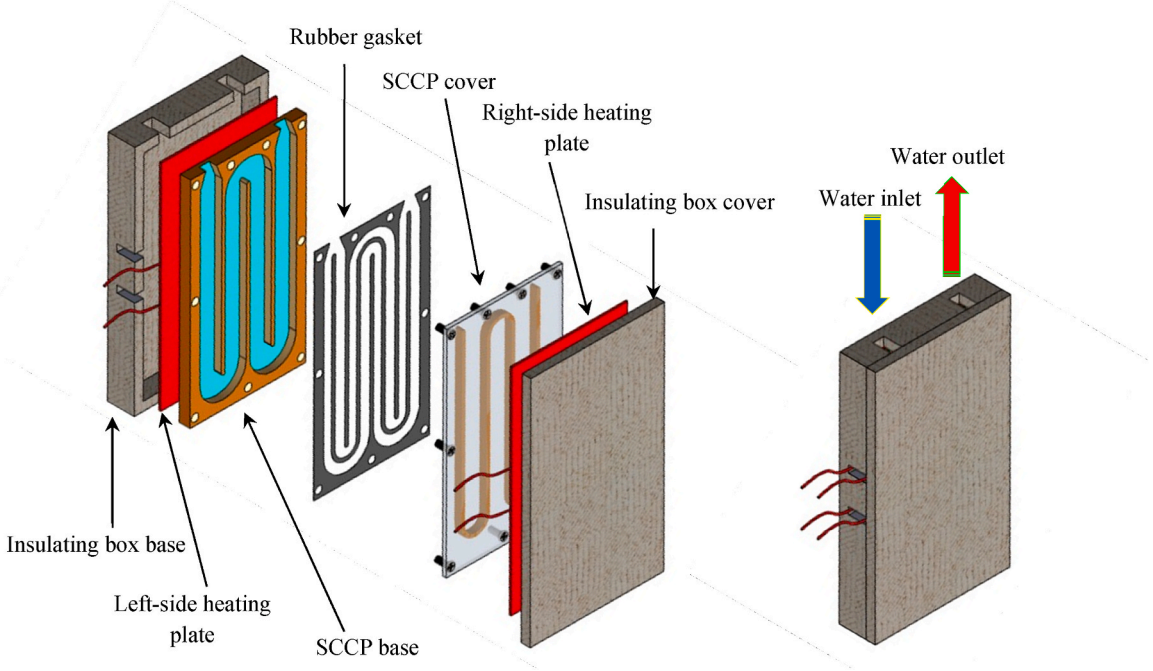

Fig. 6. Schematic illustration of the components of the manufactured SCCP assembly.

Table 3
Uncertainty estimations (E) of the performance parameters of the SCCP.

Parameter	Uncertainty calculation	Uncertainty error
E_q	$\sqrt{\left(\frac{\varepsilon\rho_f}{\rho_f}\right)^2+\left(\frac{\varepsilon Q}{Q}\right)^2+\left(\frac{\varepsilon C_{p,f}}{C_{p,f}}\right)^2+\left(\frac{\varepsilon(T_{f,o}-T_{f,i})}{(T_{f,o}-T_{f,i})}\right)^2}$	±3.6%
$E_{\Delta T_{lm}}$	$\sqrt{\left(\frac{\varepsilon(T_{f,o}-T_{f,i})}{(T_{f,o}-T_{f,i})}\right)^2+\left(\frac{\varepsilon(\overline{T_s}-T_{f,i})}{(\overline{T_s}-T_{f,i})}\right)^2+\left(\frac{\varepsilon(\overline{T_s}-T_{f,o})}{(\overline{T_s}-T_{f,o})}\right)^2}$	±4.36%
$E_{\overline{h}}$	$\sqrt{\left(\frac{\varepsilon q}{q}\right)^2+\left(\frac{\varepsilon A_h}{A_h}\right)^2+\left(\frac{\varepsilon\Delta T_{lm}}{\Delta T_{lm}}\right)^2}$	±5.65%
$E_{\overline{Nu}}$	$\sqrt{\left(\frac{\varepsilon\overline{h}}{\overline{h}}\right)^2+\left(\frac{\varepsilon D_h}{D_h}\right)^2+\left(\frac{\varepsilon\lambda_f}{\lambda_f}\right)^2}$	±5.78%
E_f	$\sqrt{\left(\frac{\varepsilon\Delta P}{\Delta P}\right)^2+\left(\frac{\varepsilon D_h}{D_h}\right)^2+\left(\frac{\varepsilon L_p}{L_p}\right)^2+\left(\frac{\varepsilon\rho_f}{\rho_f}\right)^2+\left(\frac{2\varepsilon Q}{Q}\right)^2+\left(\frac{2\varepsilon A_f}{A_f}\right)^2}$	±10.61%

specific heat, outlet temperature, and inlet temperature.

The mean logarithmic temperature difference is defined as

$$\Delta T_{lm}=\frac{(\overline{T_s}-T_{f,i})-(\overline{T_s}-T_{f,o})}{ln\left(\frac{\overline{T_s}-T_{f,i}}{\overline{T_s}-T_{f,o}}\right)} \tag{7}$$

where $\overline{T}_s$ is the average SCCP surface temperature, calculated from the readings of the ten thermocouples in the SCCP base as follows:

$$\overline{T}_s=\frac{(T_{s1}+T_{s2}+\ldots+T_{s10})}{10} \tag{8}$$

The temperature uniformity of the heating surface is widely used to evaluate the thermal performance of heat sinks. In this regard, the temperature non-uniformity (TNU) was used, which is defined as the maximum difference in the surface temperatures of the SCCP [43]. A lower value of TNU indicates better thermal performance of the SCCP.

$$\Delta T=\left(T_{s,max}-T_{s,min}\right) \tag{9}$$

The friction factor is used to compare the hydraulic performance depending on the water pressure drop through the SCCP. The friction factor is calculated as follows [40]

$$f=\frac{\Delta P\,D_h}{2\,\rho_f\,\overline{u}^2\,L_p} \tag{10}$$

where ΔP is the pressure drop inside SCCP, u is the average fluid velocity, and L_p is the length of the serpentine channel path.

The use of the ribs improves the heat transfer characteristics due to the improved fluid mixing in the channels. However, the pressure drop increases due to ribs obstruction of the flow. Therefore, in order to compare the performance with the base case of a smooth channel SCCP, the overall hydrothermal performance of the ribbed SCCP can be expressed by the Performance Improvement Factor (PIF) as follows [36]:

$$PIF=\left(\frac{\overline{Nu}_r}{\overline{Nu}_b}\right)\Big/\left(\frac{f_r}{f_b}\right)^{\frac{1}{3}} \tag{11}$$

3.3. Uncertainty analysis

The uncertainty of the experimental measurements can be estimated based on the variance and inaccuracy during the measurement, as well as the errors encountered in the calibration of the measuring devices. Depending on the uncertainty in all measured independent variables, the uncertainty in the performance parameters of the SCCP is estimated using the uncertainty propagation method [44,45]. Table 3 includes a summary of the uncertainty calculations and errors of the heat gain (q), logarithmic mean temperature difference (ΔT_{lm}), convection heat transfer coefficient ($\overline{h}$), Nusselt number ($\overline{Nu}$) and friction factor (f).

4. Results and discussion

The effects of different rib designs on the SCCP performance are investigated. The performance is studied in terms of the following parameters: surface temperature uniformity, Nusselt number, friction factor, average SCCP temperature, and the performance improvement factor.

4.1. Mesh size independence test and numerical model validation

Mesh independency test was performed to select the appropriate grid size that gives accurate results within reasonable computer execution time. Six mesh sizes ranging from 2000000 to 5220000 were tested at a Reynolds number of 1000 and discharge rate of 1C. The tests included the SCCP without ribs as well as all the considered configurations of the SCCP with 45° angle, namely, the semi-circular ribs SCCP-SCR-45°, the trapezoidal ribs SCCP-TRAP-45°, and the triangular ribs SCCP-TRAN-45°. The Nusselt number and the friction factor were selected as two trade-off

Table 4
Sensitivity analysis of the effect of number of elements (n) on the Nusselt number ($\overline{Nu}$) and friction factor (f) for the different rib shapes at an angle of 45°, discharge rate 1C and Reynolds number 1000.

SCCP	n	2003401	2510056	3107717	3600122	4320481	5080542
	$\overline{Nu}$	24.317	25.812	25.894	26.096	26.149	26.152
	f	0.0201	0.0206	0.0214	0.0220	0.0221	0.0222
SCCP-SCR-45°	n	2160813	2618056	3346592	4170122	4712573	5216174
	$\overline{Nu}$	37.631	39.294	40.372	41.256	41.347	41.367
	f	0.04057	0.0411	0.0434	0.0448	0.0453	0.0453
SCCP-TRAP-45°	n	2036184	2492146	3298483	3891251	4505616	5103547
	$\overline{Nu}$	40.049	41.011	42.709	43.603	43.675	43.689
	f	0.0473	0.0489	0.0504	0.0521	0.0525	0.0526
SCCP-TRAN-45°	n	2099341	2556202	3356375	4046874	4658922	5140264
	$\overline{Nu}$	40.201	41.744	43.234	44.132	44.221	44.238
	f	0.0497	0.0507	0.0529	0.0549	0.0552	0.0553

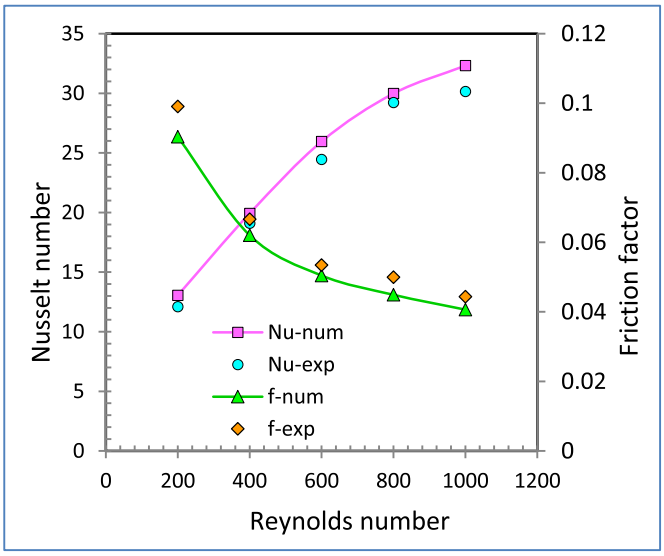

Fig. 7. Comparison between the experimentally measured (exp) and numerically predicted (num) Nusselt number (*Nu*) and friction factor (f) for the SCCP-SCR-90° under different Reynolds numbers.

criteria. The results of the tests are listed in Table 4. The mesh sizes of 4320481, 4712573, 4505616 and 4658922 are selected for all the simulations in the present study for the four SCCP types (without ribs, with 45° semi-circular ribs, with 45° trapezoidal ribs and with 45° triangular ribs, respectively).

The SCCP with 90° semi-circular ribs was experimentally tested to validate the numerical simulation model. Fig. 7 shows a comparison between the experimental and numerical results of the Nusselt number and the friction factor. Both experimental and numerical results show similar trends with maximum deviations of 8% and 11% for Nusselt number and friction factor, respectively. These deviations are due to the uncertainty in the measurements and the assumptions made in the numerical simulation. The numerical model can be accordingly used with confidence to predict the hydrothermal performance of the SCCP.

4.2. Effect of the rib orientation

The temperature distributions predicted by the numerical simulations for the smooth channel and the channel with semi-circular ribs of different orientations at a Reynolds number of 800 and a discharge rate of 1C are shown in Fig. 8. The results are drawn at a channel depth of 5 mm in the xz-plane. It can be noticed from Fig. 8 that the best heat transfer occurs at the left half of the SCCP compared with the right half since the plate temperature in the left region near the cold water inlet is lower than the right region near the water outlet from the plate. The water flowing in the channel encounters continuous increase in temperature along its path through the plate. It can be noticed that the addition of ribs enhances the heat transfer between the plate and channel. The temperature distribution on the copper plate becomes more uniform with the addition of ribs as shown in Fig. 8. The addition of ribs enhances mixing of the flow inside the channels, which results in an increase in the heat transfer. The rib angle also influences the transfer of heat. Smaller angles are more efficient than larger angles. The best temperature distribution achieved is for the SCCP-SCR-45° with a maximum of 27.46° C, which is the lowest among all the studied cases.

An important parameter in assessing the performance of a SCCP is the temperature uniformity on the heated surface. To increase the battery life, the temperature non-uniformity (TNU) on the heated surface of SCCP should be reduced as much as possible in order to reduce thermal stress. Fig. 9 indicates that in general, increasing the Reynolds number decreases TNU. On the other hand, addition of ribs reduces the dependency of TNU on the Reynolds number, especially at lower Reynolds number, since the presence of ribs improves the surface temperature. It can be seen that the temperature uniformity increases with lowering the

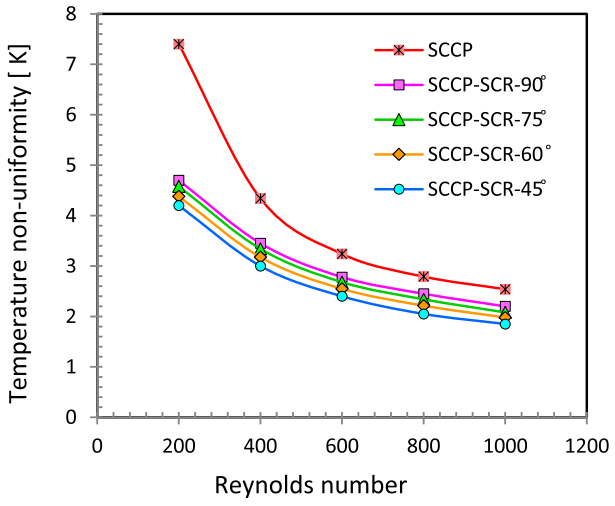

Fig. 9. Effect of the rib orientation on the temperature non-uniformity under different Reynolds numbers.

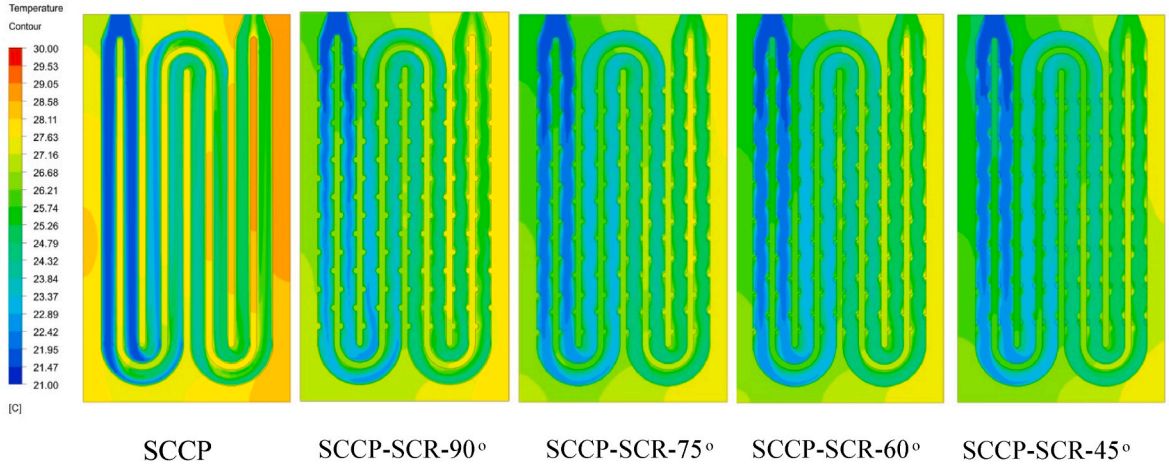

Fig. 8. Effect of the rib orientation on the temperature distribution on the SCCP.

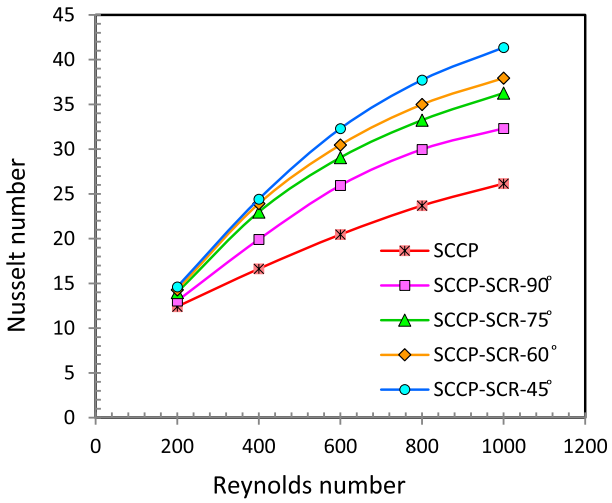

Fig. 10. Effect of the rib orientation on the Nusselt number under different Reynolds numbers.

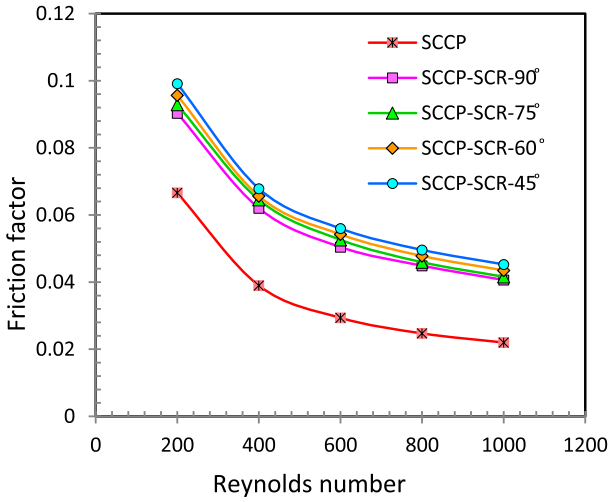

Fig. 11. Effect of the rib orientation on the friction factor under different Reynolds numbers.

rib angle. The ribs with 45° give the best uniformity among the studied cases.

Fig. 10 shows the effect of the Reynolds number on the heat transfer in terms of Nusselt with different rib orientations. The heat transfer enhancement and Nusselt number increase with increasing the Reynolds number. Adding ribs gives further improvement in the heat transfer, with ribs having smaller orientation angles being more efficient than with larger angles. The improvement is due to the generation of vortices at the intersection of each pair of ribs, which improves flow mixing and resulting in higher heat transfer. Fig. 10 indicate that at the maximum Reynolds number of 1000, the percentage increase in the Nusselt number is 29%, 45%, 52%, and 58% for SCCP-SCR-90°, SCCP-SCR-75°, SCCP-SCR-60°, and SCCP-SCR-45°, respectively, compared with the smooth SCCP.

The friction factor is an important parameter that has a significant effect on the hydraulic performance of the water flow in the channel. Fig. 11 shows the effect of the rib orientation on the friction factor at different Reynolds numbers. In all rib orientations, an exponential decline in the friction factor is observed with the increase in the

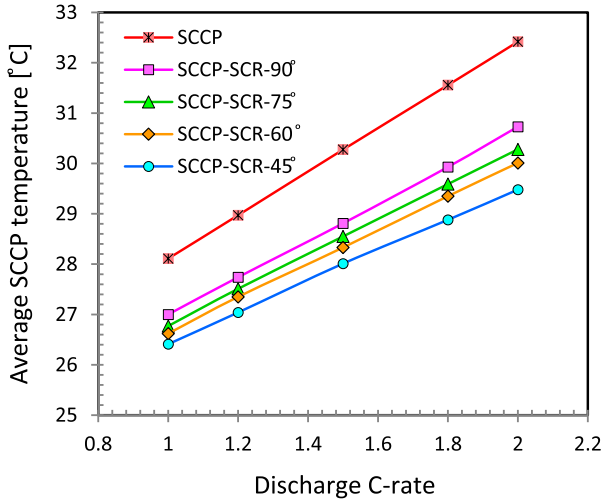

Fig. 12. Effect of the rib orientation on the average SCCP temperature under different discharge C-rates.

Reynolds number. However, the addition of ribs causes an increase in the friction factor. This is an inevitable side effect in most heat transfer enhancement techniques. The pressure drop inside the SCCP increases as the orientation angle decreases due to increased fluid mixing and intense vortex generation in the center of the channel at the intersection of each pair of ribs as a result of continuous water collision with skewed ribbed surfaces along the channel. The length of the extension of the rib on the internal surface of the channel is longer with the smaller orientation angle as was described in Fig. 3(b), which contributes in increasing the pressure drop. The maximum friction factor is produced by the 45° rib angle. A similar behavior was obtained by Tanda and Satta [36] when they compared the performance of inclined ribs at 45° angle with traditional ribs. Fig. 11 indicates that at the maximum Reynolds number of 1000, the percentage increase in the friction factor is 85%, 89%, 98%, and 106% for SCCP-SCR-90°, SCCP-SCR-75°, SCCP-SCR-60°, and SCCP-SCR-45°, respectively, compared with the smooth SCCP.

The average SCCP temperature is another important factor that relates to the thermal performance of the SCCP. The reduction of the SCCP average temperature will result in improving the dissipation of the excess heat from the battery. The effect of the rib orientations on the average SCCP temperature for the different discharge C-rates is shown in Fig. 12. In all rib orientations, a linear increase in the average SCCP temperature is observed with increasing the discharge C-rate. The temperature increase is an indication of heat accumulation inside the battery.

As was previously explained in Fig. 8, the inclusion of ribs causes a remarkable decrease in the maximum SCCP temperature and in the average SCCP temperature. The orientation angle of the ribs also affects the heat transfer and the maximum surface temperature. The ribs with the lower angles produce lower maximum surface temperature and lower average SCCP temperature. Fig. 12 indicates that at 2C-rate, the average SCCP temperature is reduced by 5.2%, 6.6%, 7.4%, and 9.1% for SCCP-SCR-90°, SCCP-SCR-75°, SCCP-SCR-60°, and SCCP-SCR-45°, respectively, compared with the smooth SCCP.

It can be concluded from the above that the addition of ribs has a positive effect on enhancing the heat transfer from the SCCP to the channel. However, the ribs cause an increase in the friction factor and a degradation of the hydraulic performance. In order to determine the overall hydrothermal performance of the SCCP, the Performance Improvement Factor (PIF) [46] is evaluated according to Eq. (11). The effect of the rib orientation on the PIF for the different values of Reynolds number is shown in Fig. 13. The PIF keeps increasing with the Reynolds number to the value of 600, after which, the PIF slightly

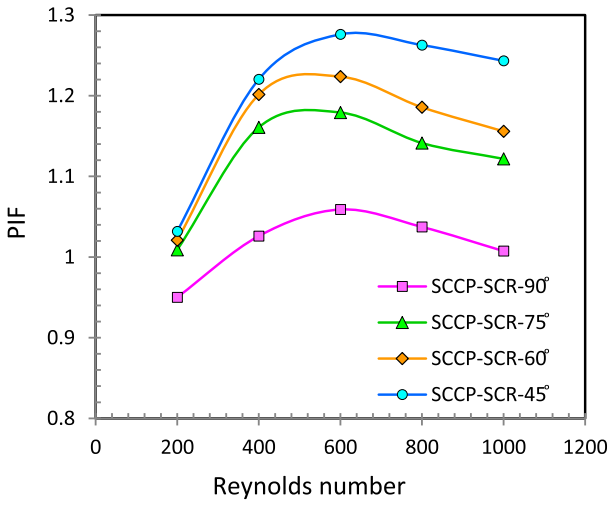

Fig. 13. Effect of the rib orientation on the performance improvement factor (PIF) under different Reynolds numbers.

decreases, meaning that the improvement in the heat transfer is dominant for Reynolds number lower than 600 but the increase in the friction factor is dominant for Reynolds number higher than 600. The ribs with lower orientation angle have higher PIF values. For the case of SCCP-SCR-90°, the value of PIF is less than 1 for Reynolds number lower than 300. The highest PIF is 1.273 for the SCCP-SCR-45° at 600 Reynolds number.

4.3. Effect of the rib shapes

According to the previous section, it can be concluded that the best thermal and combined thermal-hydraulic performance of the serpentine channel cooled plate (SCCP) is with an orientation angle of 45°. In this section, the angle is fixed at 45° but the effect of the shape of the rib (semi-circular SCR, trapezoidal TRAP, and triangular TRAN) is examined.

Fig. 14 shows the temperature distribution on the SCCP of the xz-plane at a depth of 5 mm for the smooth wall and the rib-mounted-wall with rib angle of 45° and different shapes. In all cases, the maximum temperature of the SCCP is near the water outlet due to the increase in the water temperatures as it passes through the channel. As mentioned in the previous section, adding rib makes the temperature distribution on the SCCP more uniform, which is also noted in Fig. 14 for the different rib shapes. Among the studied cases, SCCP-TRAN-45° has the best uniformity of temperature distribution.

Fig. 15 illustrates the impact of the rib shape on the surface Temperature Non-uniformity (TNU) of the SCCP for different Reynolds numbers. It can be observed that the difference in the TNU between the three shapes of the rib is small. At a Reynolds number of 200, the percentage reduction in the TNU is 43%, 45%, and 49% for the SCCP-SCR-45°, SCCP-TRAP-45° and SCCP-TRAN-45°, respectively, compared with the smooth SCCP. The SCCP-TRAN-45° has a smaller TNU.

The effect of the rib shape on the Nusselt number under different Reynolds numbers is depicted in Fig. 16. As displayed in the figure, for all rib shapes, there is a considerable heat transfer enhancement proportional to the Reynolds number. The triangular rib shape provides a small increase in Nusselt number over the two other rib shapes. The triangular ribs has a sharp edge that can strongly reverse and re-mix the flow causing periodic breaking of the thermal boundary. On the other hand, the trapezoidal rib has a small heat transfer enhancement over the semi-circular rib. At the maximum Reynolds number of 1000, the percentage enhancement in the Nusselt number is 58%, 67%, and 71% for the SCCP-SCR-45°, SCCP-TRAP-45° and SCCP-TRAN-45°, respectively,

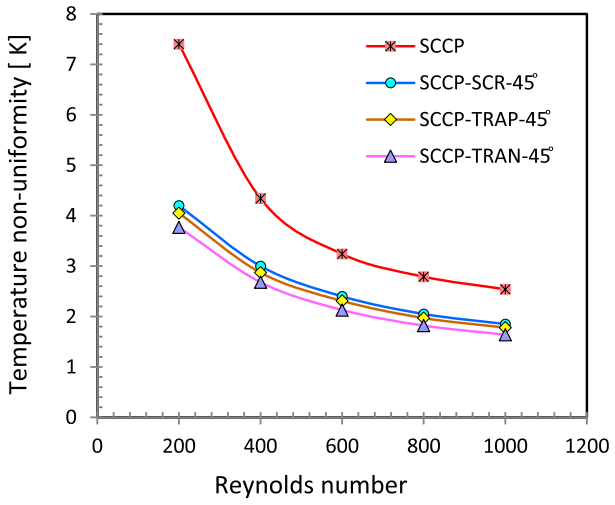

Fig. 15. Effect of the rib shape on the temperature non-uniformity under different Reynolds numbers.

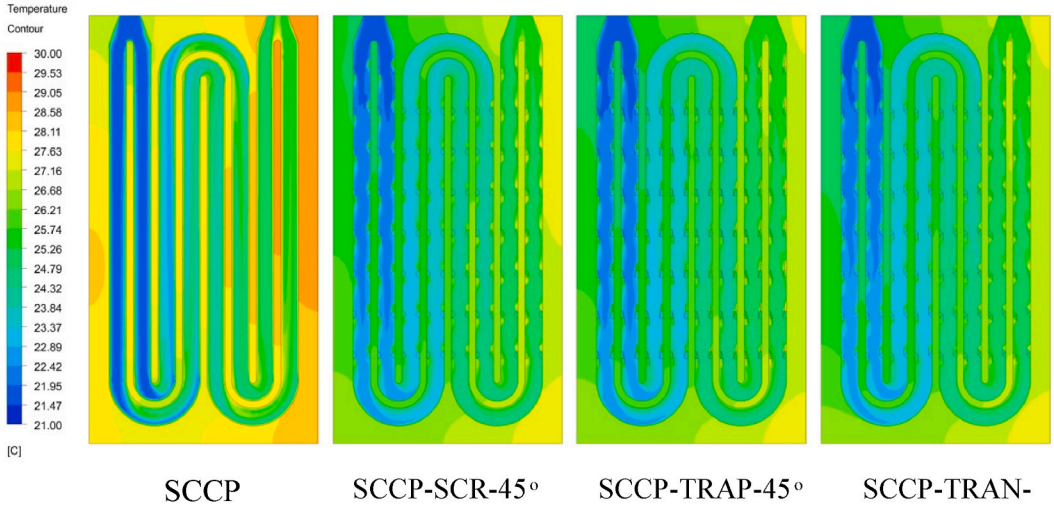

Fig. 14. Effect of the rib shape on the temperature distributions on the SCCP.

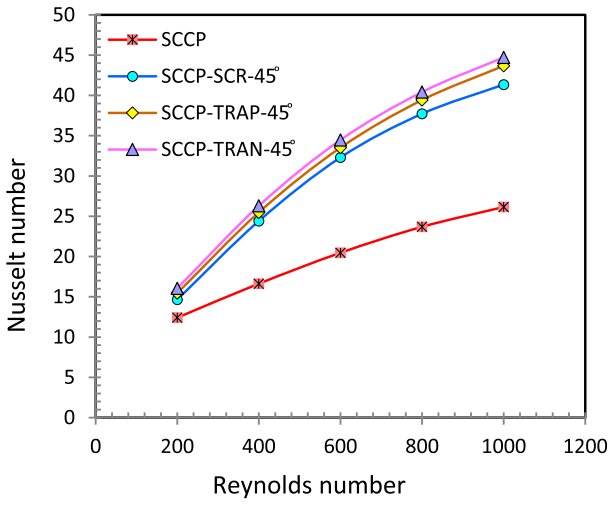

Fig. 16. Effect of the rib shape on the Nusselt number under different Reynolds numbers.

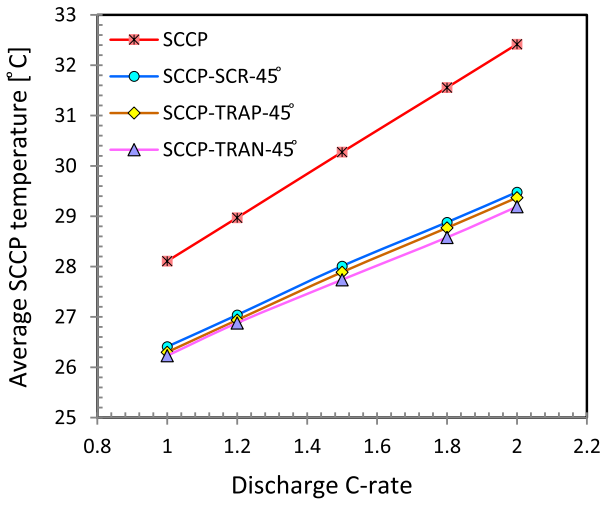

Fig. 18. Effect of rib shape on the average SCCP temperature under different discharge C-rates.

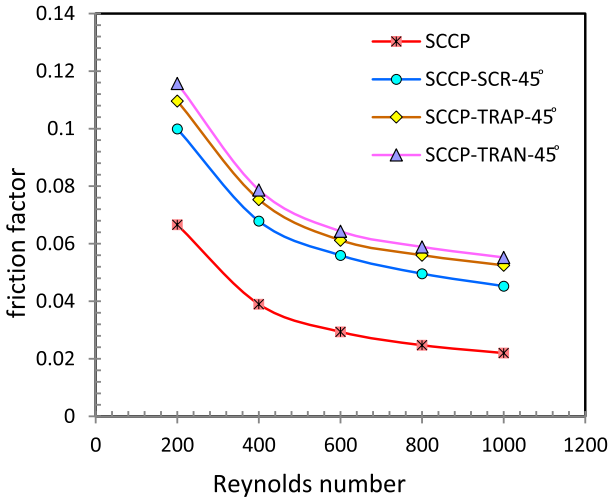

Fig. 17. Effect of the rib shape on the friction factor under different Reynolds numbers.

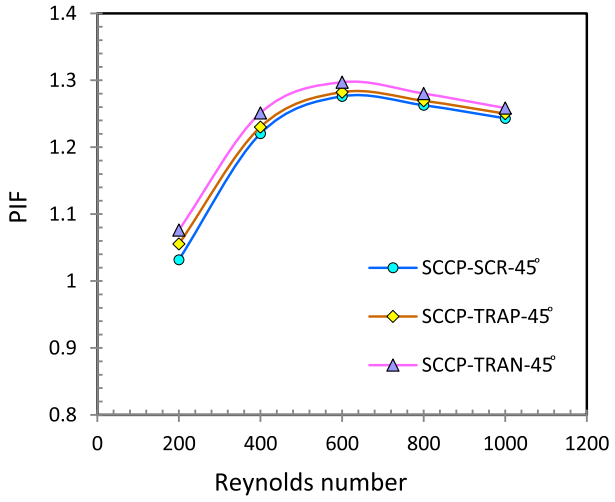

Fig. 19. Effect of the rib shape on the performance improvement factor (PIF) under different Reynolds numbers.

compared with the smooth SCCP.

The effect of the rib shape on the friction factor under different Reynolds numbers is shown in Fig. 17. As a result of its sharp edge, the greatest impediment to the flow is the triangular rib, which is reflected as increase in the friction factor in Fig. 17. At the maximum Reynolds number of 1000, the percentage increase in the friction factor is 106%, 136%, and 151% for the SCCP-SCR-45°, SCCP-TRAP-45°, and SCCP-TRAN-45°, respectively, compared with the smooth SCCP.

In Fig. 18, the effect of the rib shape on the average SCCP temperature under different discharge C-rate is illustrated. The average SCCP temperature increases with the increase in the discharge C-rate as was explained in Fig. 12. When comparing the three types of rib shapes, a slight difference in the average SCCP temperature can be observed. The lowest average SCCP temperature is that for the triangular shape and the highest is that for the semi-circular shape. It is worthwhile mentioning that the maximum average SCCP temperature for the smooth SCCP is close to 33° C and for the ribbed SCCPs is close to 29° C.

The effect of the rib shape on the overall Performance Improvement Factor (PIF) under different Reynolds numbers is shown in Fig. 19. For all shapes of the rib, a noticeable increase in the PIF is observed with the increase in the Reynolds number until reaching a Reynolds number of 600, after which it begins to slightly decrease as was previously observed in Fig. 13. It is worth noting that the PIF values with the Reynolds number for the three rib shapes are very close, with the triangular rib having a slightly better performance than the other shapes. Compared with the smooth channel SCCP, it is noticed that the maximum PIF reaches about 1.3 for SCCP-TRAN-45°. In Fig. 13, the PIF values for the different rib orientation angles showed a clear variation with the Reynolds number.

According to the above results, it can be deduced that the rib orientation angle is more effective than the rib shape in the performance enhancement of the SCCP.

5. Conclusions

In this investigation, a novel opposite oriented ribs on the walls of SCCP are proposed for the improvement of Li-ion battery cooling. Numerical modeling of the SCCP was performed under laminar water flow

conditions. The numerical simulation results were validated by comparison against experimental performance results of the manufactured SCCP. In addition to studying the effect of the operational parameters, which are the Reynolds number (from 200 to 1000) and the discharge C-rate of the battery (from 1C to 2C), the effect of the design parameters, which are the angle of rib orientation (90^{o}, 75^{o}, 60^{o}, and 45^{o}) and the shape of the rib (semi-circle, trapezoidal, and triangle) were studied. The expected benefit from the use of ribs is to interrupt the flow and produce an increase in the fluid mixing. Additionally the oriented ribs at different angles act as vortex generators inside the channel, which results in an improvement in the heat transfer characteristics of the SCCP. The numerical simulation model was validated by comparing it with the experimental results for the semi-circular ribs with 90^{o}, which showed good agreement in the performance trends and the measurements results with a maximum deviation of 11% for the friction factor and 8% for the Nusselt number.

A number of important conclusions can be drawn from this study:

1. The temperature uniformity along the SCCP is highly dependent on the channel enhancement. The temperature uniformity is better for a ribbed channel than for a smooth channel under the same operating conditions.
2. The rib orientation is more effective in reducing the maximum surface temperature of the SCCP compared with the rib shape.
3. The angle of orientation of the rib plays an important role in improving the thermal performance: the Nusselt number enhances as the angle of orientation decreases. The percentage increase in the Nusselt number reached 58% for SCCP-SCR-45^{o}.
4. It is noted that for the rib with 45^{o} angle, the triangular shape SCCP-TRAN-45^{o} has the best heat transfer improvement compared with the semi-circular and trapezoidal ribs. The percentage of improvement in the Nusselt number reached 71% for SCCP-TRAN-45^{o}.
5. For SCCP-TRAN-45^{o}, it is noticed that the increase in the overall hydrothermal performance improvement factor reaches 30% compared to the smooth channel SCCP.

Declaration of competing interest

The authors declare that they have no known competing financial interests or personal relationships that could have appeared to influence the work reported in this paper.

Data availability

Data will be made available on request.

References

[1] Y. Lai, W. Wu, K. Chen, S. Wang, C. Xin, A compact and lightweight liquid-cooled thermal management solution for cylindrical lithium-ion power battery pack, Int. J. Heat Mass Tran. 144 (2019), 118581.

[2] C. Zhao, W. Cao, T. Dong, F. Jiang, Thermal behavior study of discharging/charging cylindrical lithium-ion battery module cooled by channeled liquid flow, Int. J. Heat Mass Tran. 120 (2018) 751–762.

[3] Z. Shang, H. Qi, X. Liu, C. Ouyang, Y. Wang, Structural optimization of lithium-ion battery for improving thermal performance based on a liquid cooling system, Int. J. Heat Mass Tran. 130 (2019) 33–41.

[4] D. Chen, J. Jiang, G. Kim, C. Yang, A. Pesaran, Comparison of different cooling methods for lithium ion battery cells, Appl. Therm. Eng. 94 (2016) 846–854.

[5] S.K. Mohammadian, Y. Zhang, Thermal management optimization of an air-cooled Li-ion battery module using pin-fin heat sinks for hybrid electric vehicles, J. Power Sources 273 (2015) 431–439.

[6] X. Peng, C. Ma, A. Garg, N. Bao, X. Liao, Thermal performance investigation of an air-cooled lithium-ion battery pack considering the inconsistency of battery cells, Appl. Therm. Eng. 153 (2019) 596–903.

[7] H. Teng, K. Yeow, Design of direct and indirect liquid cooling systems for high-capacity, high-power lithium-ion battery packs, SAE Int. J. Altern. Powertrains 1 (2) (2012) 525–536.

[8] K. Yeow, H. Teng, M. Thelliez, E. Tan, Thermal analysis of a li-ion battery system with indirect liquid cooling using finite element analysis approach, SAE Int. J. Altern. Powertrains 5 (1) (2012) 65–78.

[9] L.H. Saw, H.M. Poon, H.S. Thiam, Z. Cai, W.T. Chong, N.A. Pambudi, Y.J. King, Novel thermal management system using mist cooling for lithium-ion battery packs, Appl. Energy 223 (2018) 146–158.

[10] L.H. Sawa, Y.J. King, M.C. Yew, T.C. Ng, W.T. Chong, N.A. Pambudi, Feasibility study of mist cooling for lithium-ion battery, Energy Proc. 142 (2017) 2592–2597.

[11] Y. Lyu, A.R.M. Siddique, S.H. Majid, M. Biglarbegian, S.A. Gadsden, S. Mahmud, Electric vehicle battery thermal management system with thermoelectric cooling, Energy Rep. 5 (2019) 822–827.

[12] Y. Lyu, A. Raihan, M. Siddique, S.A. Gadsden, S. Mahmud, Experimental investigation of thermoelectric cooling for a new battery pack design in a copper holder, Results Eng. 10 (2019), 100214.

[13] N. Javani, I. Dincer, G.F. Naterer, B.S. Yilbas, Heat transfer and thermal management with PCMs in a Li-ion battery cell for electric vehicles, Int. J. Heat Mass Tran. 72 (2014) 690–703.

[14] F. Bai, M. Chen, W. Song, Q. Yu, Y. Li, Z. Feng, Y. Ding, Investigation of thermal management for lithium-ion pouch battery module based on phase change slurry and mini channel cooling plate, Energy 167 (2019) 561–574.

[15] M. Mehrabi-kermani, E. Houshfar, M. Ashjaee, A novel hybrid thermal management for Li-ion batteries using phase change materials embedded in copper foams combined with forced-air convection, Int. J. Therm. Sci. 141 (2019) 47–61.

[16] F. Bai, M. Chen, W. Song, Z. Feng, Y. Li, Y. Ding, Thermal management performances of PCM/water cooling-plate using for lithium-ion battery module based on non-uniform internal heat source, Appl. Therm. Eng. 126 (2017) 17–27.

[17] Z. Rao, Y. Wen, J. Zhao, Thermal performance of battery thermal management system using composite matrix coupled with mini-channel, Energy Storage 1 (3) (2019) 1–10.

[18] Z. An, X. Chen, L. Zhao, Z. Gao, Numerical investigation on integrated thermal management for a lithium-ion battery module with a composite phase change material and liquid cooling, Appl. Therm. Eng. 163 (2019), 114345.

[19] C. Zhang, Z. Xia, B. Wang, H. Gao, S. Chen, S. Zong, K. Luo, A li-ion battery thermal management system combining a heat pipe and thermoelectric cooler, Energies 13 (841) (2020) 1–15.

[20] H. Li, X. Ding, D. Jing, M. Xiong, F. Meng, Experimental and numerical investigation of liquid-cooled heat sinks designed by topology optimization, Int. J. Therm. Sci. 146 (2019), 106065.

[21] M. Pan, X. Zhong, G. Dong, P. Huang, Experimental study of the heat dissipation of battery with a manifold micro-channel heat sink, Appl. Therm. Eng. 163 (2019), 114330.

[22] H. Xiao, Z. Liu, W. Liu, Conjugate heat transfer enhancement in the mini-channel heat sink by realizing the optimized flow pattern, Appl. Therm. Eng. 182 (2021), 116131.

[23] Y. Huo, Z. Rao, X. Liu, J. Zhao, Investigation of power battery thermal management by using mini-channel cold plate, Energy Convers. Manag. 89 (2015) 387–395.

[24] Z. Qian, Y. Li, Z. Rao, Thermal performance of lithium-ion battery thermal management system by using mini-channel cooling, Energy Convers. Manag. 126 (2016) 622–631.

[25] K. Monika, C. Chakraborty, S. Roy, S. Dinda, S.A. Singh, S.P. Datta, Parametric investigation to optimize the thermal management of pouch type lithium-ion batteries with mini-channel cold plates, Int. J. Heat Mass Tran. 164 (2021), 120568.

[26] J. Shen, Y. Wang, G. Yu, H. Li, Thermal management of prismatic lithium-Ion battery with minichannel cold plate, J. Energy Eng. 146 (1) (2020), 04019033.

[27] S. Panchal, R. Khasow, I. Dincer, M. Agelin-chaab, R. Fraser, M. Fowler, Thermal design and simulation of mini-channel cold plate for water cooled large sized prismatic lithium-ion battery, Appl. Therm. Eng. 122 (2017), 90-80.

[28] S.S. Madani, E. Schaltz, S.K. Kær, Thermal analysis of cold plate with different configurations for thermal management of lithium-ion battery, Batteries 6 (17) (2020) 1–11.

[29] L. Sheng, L. Su, H. Zhang, K. Li, Y. Fang, W. Ye, Y. Fang, Numerical investigation on a lithium ion battery thermal management utilizing a serpentine-channel liquid cooling plate exchanger, Int. J. Heat Mass Tran. 141 (2019) 658–668.

[30] S. Panchal, I. Dincer, M. Agelin-Chaab, R. Fraser, M. Fowler, Thermal modeling and validation of temperature distributions in a prismatic lithium-ion battery at different discharge rates and varying boundary conditions, Appl. Therm. Eng. 96 (2016) 190–199.

[31] T. Denga, G. Zhanga, Y. Rana, P. Liub, Thermal performance of lithium ion battery pack by using cold plate, Appl. Therm. Eng. 160 (2019), 114088.

[32] S. Chen, X. Peng, N. Bao, A. Garg, A comprehensive analysis and optimization process for an integrated liquid cooling plate for a prismatic lithium-ion battery module, Appl. Therm. Eng. 156 (2019) 324–339.

[33] B. Mondal, C.F. Lopez, A. Verma, P.P. Mukherjee, Vortex generators for active thermal management in lithium-ion battery systems, Int. J. Heat Mass Tran. 124 (2018) 800–815.

[34] T. Gao, J. Zeng, J. Zhu, J. Li, J. Gong, Effects of rib angle and rib orientation on flow and heat transfer in two-pass ribbed channels, J. Mech. Sci. Technol. 32 (1) (2018) 513–526.

[35] B. Brahim, Numerical simulation of the effect of rib orientation on fluid flow and heat transfer in rotating serpentine passages, J. Therm. Sci. Eng. Appl. 9 (2017), 011008.

[36] G. Tanda, F. Satta, Heat transfer and friction in a high aspect ratio rectangular channel with angled and intersecting ribs, Appl. Therm. Eng. 169 (2021), 120906.

[37] W. Jiang, J. Zhao, Z. Rao, Heat transfer performance enhancement of liquid cold plate based on mini V-shaped rib for battery thermal management, Int. J. Heat Mass Tran. 189 (2021), 116729.

[38] H.M. Jaffal, B. Freegah, A.A. Hussain, A. Hasan, Effect of the fluid flow fragmentation on the hydrothermal performance enhancement of a serpentine mini-channel heat sink, Case Stud. Therm. Eng. 24 (2021), 100866.
[39] A.A. Imran, N.S. Mahmoud, H.M. Jaffal, Numerical and experimental investigation of heat transfer in liquid cooling serpentine mini-channel heat sink with different new configuration models, Therm. Sci. Eng. Prog. 6 (2018) 128–139.
[40] G. Wang, T. Chen, M. Tian, G. Ding, Fluid and heat transfer characteristics of microchannel heat sink with truncated rib on sidewall, Int. J. Heat Mass Tran. 148 (2020), 119142.
[41] M.R. Sohel, S.S. Khaleduzzaman, R. Saidur, A. Hepbasli, M.F.M. Sabri, I. M. Mahbubul, An experimental investigation of heat transfer enhancement of a minichannel heat sink using Al_2O_3–H_2O nanofluid, Int. J. Heat Mass Tran. 74 (2014) 164–172.
[42] E. Hosseinirad, M. Khoshvaght-aliabadi, F. Hormozi, Effects of splitter shape on thermal-hydraulic characteristics of plate-pin-fin heat sink (PPFHS), Int. J. Heat Mass Tran. 143 (2019), 118586.
[43] Y.T. Mu, L. Chen, Y.L. He, W.Q. Tao, Numerical study on temperature uniformity in a novel mini-channel heat sink with different flow field configurations, Int. J. Heat Mass Tran. 85 (2015) 147–157.
[44] X. Cao, H. Liu, X. Shao, H. Shen, G. Xie, Thermal performance of double serpentine minichannel heat sinks: effects of inlet-outlet arrangements and through-holes, Int. J. Heat Mass Tran. 153 (2020), 119575.
[45] S. Wiriyasart, P. Naphon, Heat spreading of liquid jet impingement cooling of cold plate heat sink with different fin shapes, Case Stud. Therm. Eng. 20 (2020), 100638.
[46] N.S. Mahmoud, H.M. Jaffal, A.A. Imran, Performance evaluation of serpentine and multi-channel heat sinks based on energy and exergy analyses, Appl. Therm. Eng. 186 (2021), 116475.